

# Crossover from Karplus-Luttinger to Topological Hall Effects in SrRuO<sub>3</sub>-based heterostructures

Z. S. Lim<sup>1</sup>, L. E. Chow<sup>1</sup>, P. Yang<sup>2</sup>, G. J. Omar<sup>1</sup>, Z. Zhang<sup>1</sup>, A. Ariando<sup>1</sup>

1. Physics Department, Block S12, #2 Science Drive 3, National University of Singapore 117551

2. Singapore Synchrotron Light Source, 5 Research Link, Buona Vista, Singapore 117603

## Abstract:

Using SrRuO<sub>3</sub>-based thin film heterostructures, we aim to resolve the two debated interpretations that distinguish between the genuine Topological Hall Effect (THE) and the artefactual humps produced from overlapping double Karplus-Luttinger Anomalous Hall Effects (KL-AHE), without magnetic imaging. Firstly, we selected two heterostructures with similar Hall Effect but with contrasting octahedral rotations/tilts, providing a clue to determining the presence/absence of Dzyaloshinskii-Moriya Interaction. Secondly, we employ the  $\theta$ -rotation of magnetic field from out-of-plane to in-plane as the critical judgemental tool. The first heterostructure showing field-position of Hall hump diverging with  $\sim 1/\cos(\theta)$  is correctly reproduced using the double KL-AHEs. Yet, the second one showing constant hump field versus  $\theta$  behaviour agrees with a micromagnetic simulation with Néel-Skyrmions and is thus convincingly assigned as THE. Lastly, for a general system evolving with increasing magnetic field from two-dimensional Skyrmion-lattice into collinear ferromagnetic in the real-space, we further discuss about the corresponding evolution of k-space band structure from gapped massive Dirac Fermion into Weyl Fermion, consistent to past literatures. Its associated transformation from “Mirror Anomaly” into “Chiral Anomaly” is detectable via electrical transport and further assisted in resolving the aforementioned debate. We hence emphasize the two schemes as useful, generic electrical measurement protocols for future search of magnetic Skyrmions.

## Article:

The motivation of stabilizing magnetic Skyrmions[1,2] in perovskite oxide thin films is well-justified since the control of Skyrmions could be extended into more robust degrees of freedom such as multiferroicity, which is beneficial for future energy-saving spintronic devices. Some celebrated examples are  $\text{Cu}_2\text{OSeO}_3$ [3-6] and the  $\text{BaTiO}_3/\text{SrRuO}_3$  heterostructures[7], where magnetic Skyrmions are directly coupled to the ferroelectric polarization. In various recent attempts for building Skyrmion-hosting thin film heterostructures in oxides or topological insulators[7-12], the Topological Hall Effect (THE) has frequently been a convenient tool for characterization, which describes the perpendicular deflection of spin-polarized electrons by magnetic Skyrmions or other textures with net scalar moment chirality (SMC)[13,14]. However, since the typical THE shape adopts a pair of antisymmetric humps with sweeping magnetic field corresponding to Skyrmion phase evolution from nucleation to annihilation, it can be reproduced numerically by two overlapping Langevin-function loops with opposite signs[15]. In contrast to Skyrmions, such “Bi-Langevin decomposition” implies inhomogeneous, topologically-trivial collinear domains with opposite signs of k-space Berry curvatures, where the Langevin functions refer to the Karplus-Luttinger Anomalous Hall Effect (KL-AHE) that follows the shape of z-component magnetization ( $M_z$ ). Yet, some authors debated that the Bi-Langevin decomposition analysis yielded neither sensible temperature-dependent trends[16], nor observable double-hysteresis in magnetometry  $M$ - $H$  loops[17], creating confusions.

This has led to increasing demand on real-space imaging techniques for convincing verification on the magnetic states; and indeed, contrasting imaging results were reported among systems sharing the similar Hall-hump features. Particularly, the magnetic force microscopy (MFM) and X-ray circular dichroism photoelectron microscopy (XMCD-PEEM) obtained irregular sized Skyrmion-like bubbles in several doped-/charge-transfer

manganites[17,18] and  $\text{SrIrO}_3/\text{SrRuO}_3$  (SIO/SRO) bilayers[19], although their exact topological charge ( $Q$ ), vorticity ( $Q_v$ ) and helicity ( $Q_h$ ) remain unknown. Whereas the single-layer SRO thin films with deliberate terrace engineering exhibited inhomogeneous domains segregated along atomic terraces[20]. By definition, a crucial difference lies in domain wall energy, which is negative for magnetic Skyrmions but positive for regular domains, as derived by Bogdanov[21,22]. Correspondingly, the SMC-generated THE does not require spin-orbit coupling (SOC) in electron deflection[23,24], and can be classified as a subset of AHE. Yet both the intrinsic KL, extrinsic skew-scattering and side-jump AHE mechanisms must involve SOC directly[25,26] in their respective perturbation Hamiltonians. Most recently, the “double- $q$  incommensurate spin-crystal (IC)” phase found in Fourier-transformed MFM images of SRO/PbTiO<sub>3</sub> bilayer still has the required SMC, supporting the notion of THE[27]. In this work, targeting the aforementioned debate, we reveal that the rotation of magnetic field direction in Hall measurements contains valuable information. Assisted by micromagnetic simulation and comparing between two selected heterostructures, the Hall-hump features show distinct behaviours that distinguish between KL-AHE for inhomogeneous trivial magnetic domains and true THE originating from genuine magnetic Skyrmions, without imaging. Furthermore, magnetic field rotation in Hall and linear resistance measurements also reveal possible signatures of crossover between massive Dirac Fermion and Weyl Fermion in the latter heterostructure, but absent in the former.

Our selected heterostructures grown on perovskite SrTiO<sub>3</sub>(001) substrates comprise combinations of SRO and SIO, with varying oxygen partial pressure ( $P_{\text{O}_2}$ ) during film growth in a pulsed laser deposition (PLD) setup. The “high/low-pressure (hp-/lp-)” prefixes correspond to  $P_{\text{O}_2}$  of 100 and 10 mTorr respectively, at a common temperature of 650°C. Firstly, it is expected that thick hp-SRO(34uc) is in monoclinic-phase, near bulk-like, with a saturation magnetization ( $M_{\text{sat}}$ ) of  $\sim 1.6 \mu_{\text{B}}/\text{Ru}$  and ferromagnetic Curie temperature ( $T_C$ ) of

$\sim$ 150 K. Its negative-sign AHE (Fig. 1a) is consistent to the well-known spin-polarization ( $P_S$ ) of -9.5%[28] and negative Chern number in its  $t_{2g}$ -dominated k-space band structure[15]. Whereas the lp-SRO is in tetragonal-phase stabilized by higher oxygen vacancy ( $V_O$ ) content, having lower  $M_{sat}$  and  $T_C$ , and positive-sign AHE (Fig. 1b), even up to a relatively large thickness (34 uc)[29,30]. These contrasting magnetic properties of SRO phases are consistent to a recent first-principle calculation[15]. Combining ultrathin films of these two phases into the hp-SRO(3uc)/lp-SRO(7uc) (sample C), strong Hall-humps can be observed (Fig. 1c). On the other hand, SrIrO<sub>3</sub> is a paramagnetic semimetal with strong SOC[31,32]. The hp-SRO(5uc)/hp-SIO(10uc) (sample D) also shows strong Hall-hump features (Fig. 1d); yet the hp-SRO(5uc)/lp-SIO(10uc) (sample E) shown in Fig. S1c only has positive-sign Langevin-shaped AHE without hump.

We refer to Fig. S1a to clarify the motivations of fabricating the mentioned heterostructures, with octahedral tilt/rotations measured by half-integer (HKL)-indices X-ray Bragg diffractions. To replicate the hump features found in single-layer SRO films recently associated with inhomogeneous trivial domains[20,33], the sample C is designed for more insightful and consistent control. This is reasonable since single-layer SRO films grown on the cubic STO(001) substrate would inevitably suffer from restriction of octahedral tilt/rotations adjacent to the substrate, up to a critical thickness beyond which strain relaxation gradually occurs; yet the critical thickness may have large variance among researchers worldwide due to slight differences in film growth conditions. The glazer notation[34] of 34 uc hp-SRO is majority  $a^-b^+c^-$  which is consistent to past reports[31,35]; but is  $a^0a^0c^0$  in both the 34 uc lp-SRO and sample C. Conversely sample D is made for mimicking reference [19] with Skyrmion-like bubbles. Its restriction of octahedral tilts/rotations and subsequent gradual relaxation occur within the hp-SIO (akin to a buffer) from  $a^0b^0c^0$  to  $a^+b^0c^0$  approaching the SRO/SIO interface, hence the top hp-SRO is more relaxed and achieves  $a^-$

$b^+c^0$  within the 5-uc thickness (Fig. S1b). While the disappearance of Hall-humps in sample E can be linked to the total suppression of  $a^+$ ,  $a^-$  and  $b^+$  resulted from the bottom lp-SIO. In summary, it is possible to deduce the presence of interface Dzyaloshinskii-Moriya Interaction (DMI)[36] in sample D due to abrupt change of octahedral tilts across the SRO/SIO interface, which is absent in C and E.

Having established the structural comprehension and their corresponding Hall Effect, we continued investigations into Hall measurement with rotation of magnetic field direction ( $\rho_{xy}(\theta, H)$ ) from out-of-plane ( $\mathbf{H} \parallel z$  at  $\theta=0^\circ$ ) to in-plane ( $\mathbf{H} \parallel y$  at  $\theta=90^\circ$ ) and 20 K. This is illustrated in Fig. 2 (top), presented in total field,  $H = \sqrt{H_z^2 + H_y^2}$ . Notably, the Hall-hump peak field ( $H_{\text{peak}}$ ) of sample C exhibits strong response, shifting to larger field with increasing  $\theta$ , nearly approaching the  $1/\cos(\theta)$  limit (Fig. 2a). The  $1/\cos(\theta)$  limit implies zero contribution from the in-plane field. This is very similar to the  $H_C$  response of hp- and lp-SRO thick films with varying  $\theta$  by measuring their AHE and magnetoresistance (MR) peaks as shown in Fig. S2a,b. A fitting for such response with  $H_C = 1/\cos^\alpha(\theta)$  yielded exponents of  $\alpha=0.74$ , 0.62 and 0.37 for samples C, B and A respectively. It is then easy to reproduce the diverging  $H_{\text{peak}}$  trend (Fig. 2c), by decomposing the Hall data of sample C at  $\theta=0^\circ$  into two opposite-sign AHE loops via Langevin function fittings incorporating the  $1/\cos^\alpha(\theta)$  scaling:  $\rho_{xy}(\theta) = \sum_{i=1,2} A_i \left\{ \coth \left[ B_i \left( H - \frac{H_{C,i}(\theta=0)}{\cos^{0.74}(\theta)} \right) \right] - \left[ B_i \left( H - \frac{H_{C,i}(\theta=0)}{\cos^{0.74}(\theta)} \right) \right]^{-1} \right\}$ , where  $A_i$  and  $B_i$  are saturation AHE and loop squareness coefficients. Such  $\theta$ -dependent Hall analysis, albeit unprecedented, supports that the sample C hosting trivial inhomogeneous domains with opposite-sign KL-AHEs at intermediate fields in agreement to reference [20], unrelated to Skyrmions.

However, the  $H_{\text{peak}}$  of sample D is almost independent of  $\theta$  (with  $\alpha \sim 0.06$ ) as shown in Fig. 2b, thus the possible existence of real magnetic Skyrmions cannot be ruled out. We then performed MUMAX<sup>3</sup> micromagnetic simulations[37] (Fig. S4) by using realistic parameters

extracted from magnetometry (Fig. S3), except induced interface DMI ( $D_{\text{ind}}$ ) is allowed as a free parameter for matching the simulated peak topological charge density ( $TCD$ ) =  $\frac{1}{4\pi} \hat{\mathbf{m}} \cdot \left( \frac{\partial \hat{\mathbf{m}}}{\partial x} \times \frac{\partial \hat{\mathbf{m}}}{\partial y} \right)$  to the Hall-hump's  $H_{\text{peak}}$  at  $\theta=0^{\circ}$ , assuming they are the genuine THE emanating from Néel-type magnetic Skyrmions. At a reasonable  $D_{\text{ind}}$  of  $1.85 \times 10^{-3}$  J/m<sup>2</sup> for peak  $TCD$  at  $\mu_0 H \sim 1.0$  T, we obtained a mapping of  $TCD(\theta, H)$ , showing that the total field corresponding to the densest Skyrmion-lattice (SkL) maintains almost constant with increasing  $\theta$  (Fig. 2d). Following the general Landau-Ginzburg framework for triple- $\mathbf{q}$  spin-waves superposition, it is well-known that helicoidal waves  $\mathbf{m}_i = \sum_i^{1,2,3} [\mathbf{m}_z \cos(\mathbf{k}_i \cdot \hat{\mathbf{r}}) + (\mathbf{m}_z \times \mathbf{k}_i) \sin(\mathbf{k}_i \cdot \hat{\mathbf{r}})]$  would create a two-dimensional (2D) hexagonal-close-packed Bloch-type SkL and cycloidal waves  $\mathbf{m}_i = \sum_i^{1,2,3} [\mathbf{m}_z \cos(\mathbf{k}_i \cdot \hat{\mathbf{r}}) + k_i \sin(\mathbf{k}_i \cdot \hat{\mathbf{r}})]$  for Néel-SkL, where  $\hat{\mathbf{r}} = [\hat{\mathbf{x}}, \hat{\mathbf{y}}, \hat{\mathbf{z}}]$ ,  $\mathbf{m}_z = [0, 0, 1]$ , and  $\mathbf{k}_i = \left[ \cos\left(\frac{2\pi i}{3}\right), \sin\left(\frac{2\pi i}{3}\right), 0 \right]$ . Subsequent sign-reversal from the helicoidal/cycloidal superposition with either  $x \rightarrow -x$  or  $y \rightarrow -y$  would create Antiskyrmion-lattices. Hence the simulation result above becomes intuitive – an additional in-plane field component would cause dominance of one of the three spin-waves and destroy the SkLs[38,39], instead of no contribution.

Next, it is interesting to discuss about the evolution of k-space band structure following the topological magnetic phase transition. It is well-known that from an effective magnetic Hamiltonian of a typical Skyrmion-hosting material with competing interactions including exchange stiffness, anisotropy, DMI and Zeeman term, the Skyrmion phase-space exists at elevated temperatures due to weakened exchange relative to DMI. With increasing magnetic field, the magnetic phase transforms from single- $\mathbf{q}$  helicoids/cyloids into triple- $\mathbf{q}$  SkL, before saturating into collinear ferromagnetic (FM). The low-field phases are not multi-domain FM and thus are not expected to share the same k-space band structure as the high-field collinear FM; yet such information is hardly accessible from *ab-initio* density functional

theory (DFT) calculations due to being high-temperature excitations and involving large magnetic unit-cell. Recently, tight-binding models on either a 2D honeycomb- or square-SkL have revealed the existence of gapped Dirac Fermion near the Fermi surface ( $E_F$ ), with THE can be directly calculated from Kubo formula[40,41]. This is with condition that the electron mean free path is long compared to the SkL unit-cell for practical computational cost, otherwise the semi-classical effective magnetic field picture preferred[14]. On the other hand, the type-II Dirac semimetal (DSM) has been theorized by Burkov et al. to possess “mirror anomaly” due to their 2D nature, which is detectable via  $\rho_{xy}(\theta, H)$  as step functions across the 2D mirror plane at  $\theta=\pm 90^\circ$  and/or other time-reversal-invariant momenta (TRIM)[42,43]. If breaking the time-reversal symmetry (TRS) to create pairs of Weyl-nodes, the “Adler-Bell-Jackiw’s (chiral) anomaly” would occur at  $\mathbf{H} \parallel \mathbf{I}$  alignment of the anisotropic magnetoconductivity (AMC) measurement[44-48]. Here, we show the crossover between the two anomalies detected by field rotations.

In Fig. 2e,f, we compare between the sample C and D using the same  $\rho_{xy}(\theta, H)$  scheme. In sample D at  $\mu_0 H = \mp 1.0$  T after  $\pm 9$  T corresponding to  $H_{\text{peak}}$ , sharp step functions occur at  $\theta = \sim \pm 30^\circ$ ,  $\sim \pm 90^\circ$  and  $\sim \pm 150^\circ$  with obvious hysteresis. Those steps are qualitatively similar in  $\rho_{xy}(\beta, H)$  for field rotation in the xz-plane, and with varying temperatures (Fig. S2c). The  $\pm 90^\circ$  steps can be assigned as the parity anomaly across the xy-mirror plane, while the steps at  $\pm 30^\circ$  and  $\pm 150^\circ$  likely originate from extra TRIMs in the honeycomb SkL. Note that such hysteretic steps at  $\theta = \sim \pm 45^\circ$  and  $\sim \pm 135^\circ$  also occurred in THE measurement of the moderately frustrated  $\text{Gd}_2\text{PdSi}_3$  with rotating-field in reference[49]. Yet no step-function can be found at  $H_{\text{peak}}$  of sample C located at approximately  $\mu_0 H = \mp 0.7$  T after  $\pm 5$  T saturation. At large fields corresponding to collinear FM saturation, step function is absent in  $\rho_{xy}(\theta)$  for both C and D. For sample E without humps, all step-functions vanish at both small and large fields (Fig. S2d). This way, we can infer that sample D shows the “mirror anomaly” as a characteristic

property of gapped massive Dirac Fermion in k-space (in agreement to existence of 2D-SkL in real-space), which vanishes at large field for collinear FM. We note that such claim may be ambitious if without a band structure mapping by Angle-resolved Photoelectron Emission Spectroscopy (ARPES).

We then discuss the final aspect – xy-plane AMC ( $\sigma_{xx}(\gamma, H)$ ) as defined at the top schematic of Fig. 3 – for identifying the chiral anomaly of 3D Weyl Fermion. The  $\gamma$ -rotation was chosen to exclude the out-of-plane field and rule out the perpendicular magnetic anisotropy (PMA) contribution, while in-plane magnetocrystalline anisotropy should be fourfold-symmetric due to the cubic SrTiO<sub>3</sub>(001) substrate used. In sample C, the  $\sigma_{xx}(H)$  is positive and parabolic at both  $\mathbf{H} \perp \mathbf{I}$  ( $\gamma=0^\circ$ ) and  $\mathbf{H} \parallel \mathbf{I}$  ( $\gamma=90^\circ$ ) (Fig. 3a), and is possibly a type-II Weyl Fermion behaviour. Continuous  $\gamma$ -rotation creates a twofold-symmetric sinusoidal curve at all fields with no sharp kinks (Fig. 3c), implying the Fermi surface is still far away from being a Weyl-semimetal (WSM) regime. Since the orbital (Lorentz force) scattering contribution should be absent at  $\mathbf{H} \parallel \mathbf{I}$ , its higher  $\sigma_{xx}$  compared to  $\mathbf{H} \perp \mathbf{I}$  cannot be unambiguously assigned as the chiral anomaly phenomenon. On the other hand, sample D shows linear positive  $\sigma_{xx}(H)$  at  $\mathbf{H} \parallel \mathbf{I}$  but negative  $\sigma_{xx}(H)$  at  $\mathbf{H} \perp \mathbf{I}$  (Fig. 3b), while continuous  $\gamma$ -rotation yields sharp kinks at  $\mathbf{H} \parallel \mathbf{I}$  at high fields (Fig. 3d). These behaviours at high field are consistent to a WSM’s “chiral anomaly” behaviour due to its high sensitivity to parallel  $\mathbf{H} \parallel \mathbf{I}$  alignment[50,51]; yet reducing field causes the kinks to smoothen. However, quantum oscillation is unlikely accessible, due to low electron mobility for PLD-grown samples, in contrast to reference [52].

Combining the evidences in Fig. 2e,f and 3, sample D can be convincingly ascribed to having a 2D-SkL in real-space with THE and gapped massive Dirac Fermion in k-space at low field, but transforming into a FM Weyl-Fermion at high field. Whereas sample C only has topologically-trivial FM domains showing double KL-AHE at low field. This work not

only resolves the previously lingering debate but also bridges the gap in understanding the k-space band structure of magnetic Skyrmion lattice. As a final remark, we noticed the chemical instability of sample C upon inevitable exposure to air and moisture, likely due to oxygen vacancy migration from the bottom lp-SRO to the top hp-SRO following its concentration gradient. Thus, only data from freshly-made samples C with noticeable Hall-humps were analysed above, since its positive KL-AHE component contributed by the lp-SRO would gradually dominate leading to vanished Hall-humps within a few days. Yet sample D is stable in air since the more chemically-sensitive SIO layer is sandwiched and unexposed.

### References:

- [1] Nagaosa *et al.*, Nat. Nanotechnol. **8**, 899 (2013).
- [2] Zhang *et al.*, J. Phys.: Condens. Matter **32**, 143001 (2020).
- [3] Seki *et al.*, Science **336**, 198 (2012).
- [4] Seki *et al.*, Phys. Rev. B **86**, 060403 (2012).
- [5] Okamura *et al.*, Nat. Commun. **4**, 2391 (2013).
- [6] Okamura *et al.*, Nat. Commun. **7**, 12669 (2016).
- [7] Wang *et al.*, Nat. Mater. **17**, 1087 (2018).
- [8] Matsuno *et al.*, Sci. Adv. **2**, e1600304 (2016).
- [9] Yasuda *et al.*, Nat. Phys. **12**, 555 (2016).
- [10] Wang *et al.*, Nat. Mater. **18**, 1054 (2019).
- [11] Shao *et al.*, Nat. Electron. **2**, 182 (2019).
- [12] Ahmed *et al.*, Nano Lett. **19**, 5683 (2019).
- [13] Tatara *et al.*, J. Phys. Soc. Jpn. **71**, 2613 (2002).
- [14] Bruno *et al.*, Phys. Rev. Lett. **93**, 096806 (2004).
- [15] Groenendijk *et al.*, Phys. Rev. Res. **2**, 023404 (2020).
- [16] Li *et al.*, Nano Lett. **21**, 84 (2021).
- [17] Skoropata *et al.*, Sci. Adv. **6**, eaaz3902 (2020).
- [18] Vistoli *et al.*, Nat. Phys. **15**, 67 (2019).
- [19] Meng *et al.*, Nano Lett. **19**, 3169 (2019).
- [20] Wang *et al.*, Nano Lett. **20**, 2468 (2020).
- [21] Bogdanov *et al.*, JETP **95**, 178 (1989).
- [22] Bogdanov *et al.*, JMMM **138**, 255 (1994).
- [23] Zhang *et al.*, Phys. Rev. B **95**, 075128 (2017).
- [24] Hirschberger *et al.*, Phys. Rev. B **103**, L041111 (2021).
- [25] Karplus *et al.*, Phys. Rev. **95**, 1154 (1954).
- [26] Nagaosa *et al.*, Rev. Mod. Phys. **82**, 1539 (2010).
- [27] Seddon *et al.*, Nat. Commun. **12**, 2007 (2021).
- [28] Worledge *et al.*, Phys. Rev. Lett. **85**, 5182 (2000).
- [29] Lu *et al.*, Phys. Rev. B **88**, 214115 (2013).
- [30] Qin *et al.*, Adv. Mater. **31**, 1807008 (2019).

- [31] Nie *et al.*, Phys. Rev. Lett. **114**, 016401 (2015).
- [32] Zeb *et al.*, Phys. Rev. B **86**, 085149 (2012).
- [33] Kan *et al.*, Phys. Rev. B **98**, 180408 (2018).
- [34] Glazer, AcCrB **28**, 3384 (1972).
- [35] van Thiel *et al.*, ACS Materials Letters **2**, 389 (2020).
- [36] Moriya, Phys. Rev. **120**, 91 (1960).
- [37] Vansteenkiste *et al.*, AIP Advances **4**, 107133 (2014).
- [38] Leonov *et al.*, Phys. Rev. B **96**, 214413 (2017).
- [39] Wan *et al.*, Phys. Rev. B **99**, 180406 (2019).
- [40] Hamamoto *et al.*, Phys. Rev. B **92**, 115417 (2015).
- [41] Göbel *et al.*, Phys. Rev. B **95**, 094413 (2017).
- [42] Burkov, Phys. Rev. Lett. **120**, 016603 (2018).
- [43] Nandy *et al.*, Phys. Rev. B **99**, 075116 (2019).
- [44] Armitage *et al.*, Rev. Mod. Phys. **90**, 015001 (2018).
- [45] Nagaosa *et al.*, Nat. Rev. Mat. **5**, 621 (2020).
- [46] Ong *et al.*, Nature Reviews Physics **3**, 394 (2021).
- [47] Ishizuka *et al.*, Phys. Rev. B **99**, 115205 (2019).
- [48] Nielsen *et al.*, Phys. Lett. B **130**, 389 (1983).
- [49] Kurumaji *et al.*, Science **365**, 914 (2019).
- [50] Xiong *et al.*, **350**, 413 (2015).
- [51] Zhang *et al.*, Nat. Commun. **7**, 10735 (2016).
- [52] Takiguchi *et al.*, Nat. Commun. **11**, 4969 (2020).

**Figures:**

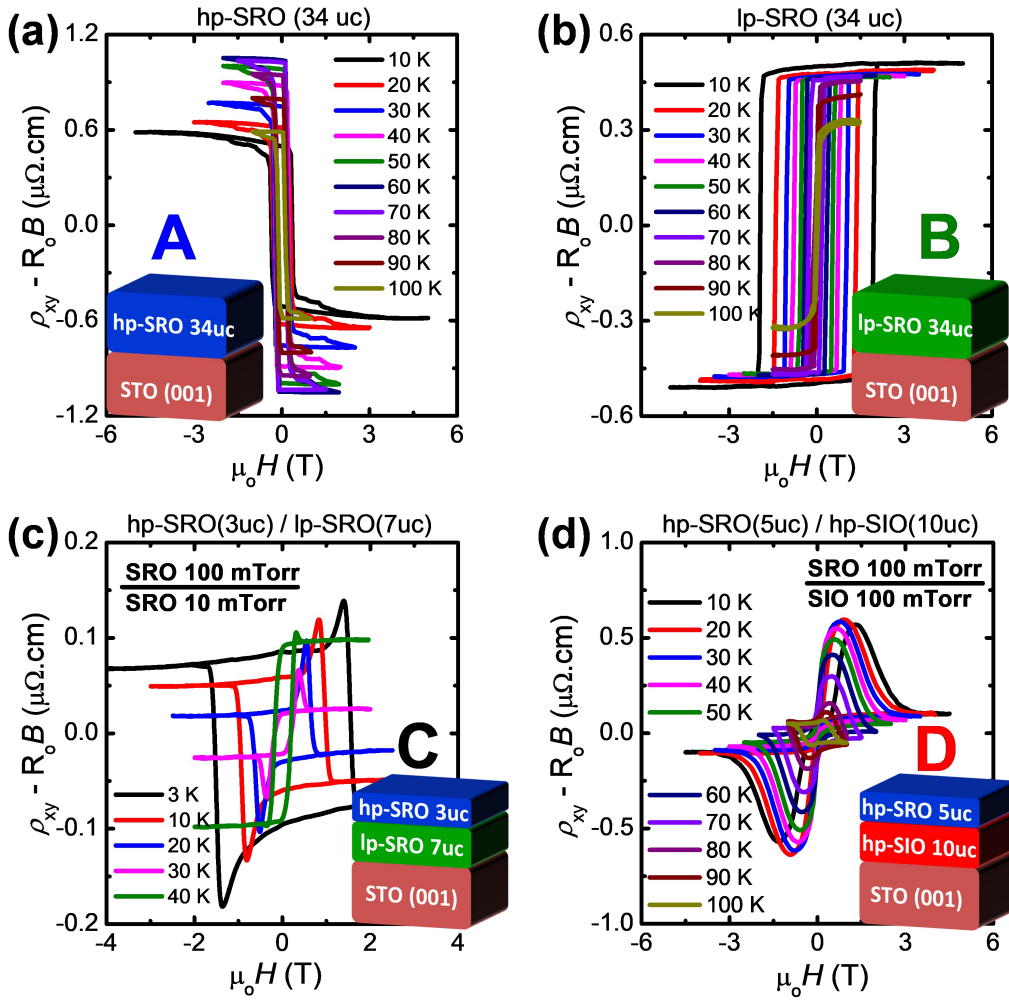


**Figure 1: (a) to (d)** Hall data of sample A, B, C, D with varying temperatures. The Ordinary Hall Effect (OHE) components were removed by linear background subtraction indicated by the “ $-R_o B$ ” term at the vertical axes’ labels.

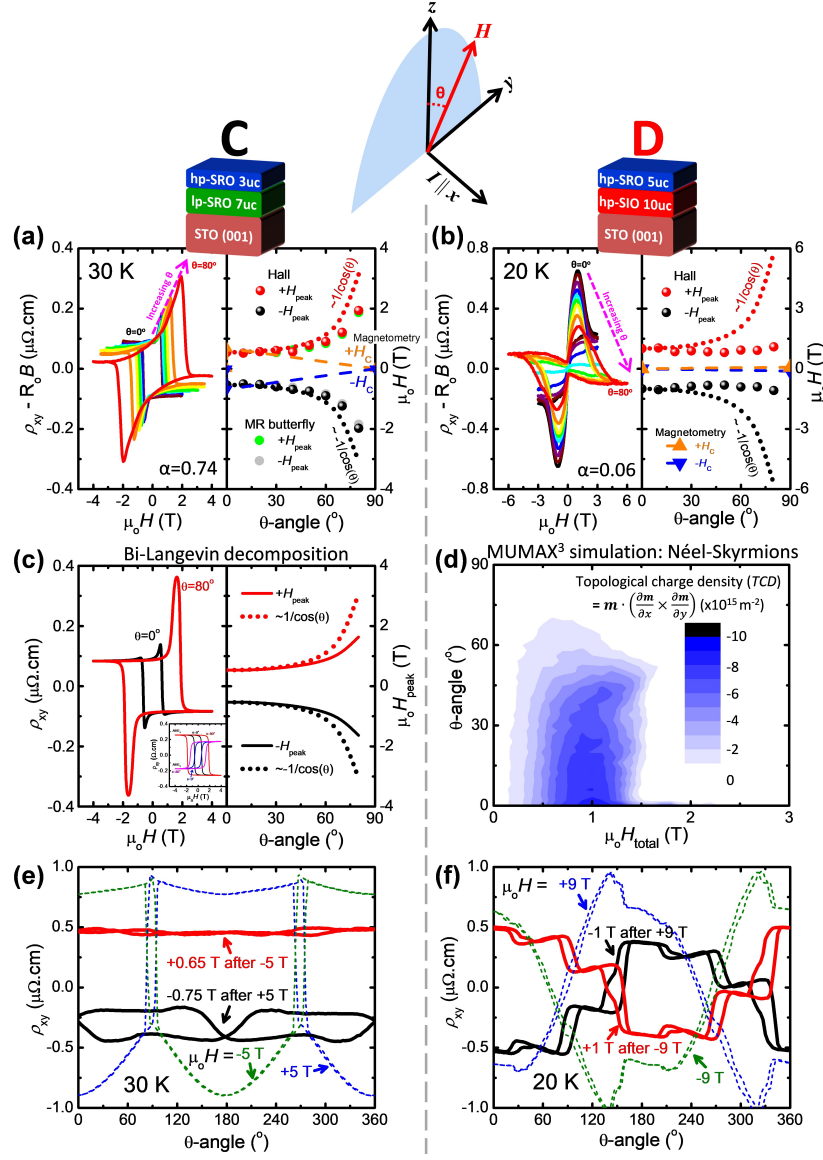


**Figure 2: Top panel:** Sketch of rotating-field Hall measurement configuration  $\rho_{xy}(\theta, H)$ . **(a, b)** Hall data (left panels) and analyses of Hall-humps  $H_{\text{peak}}$  with varying  $\theta$  (right panels) for samples C,D.  $H_{\text{peak}}$  of magnetoresistance (MR) butterfly loops (not shown) are overlapped in (a) for comparison. **(c, d)** Explanation models for the observations in (a, b) using the bi-Langevin decomposition for sample C and the MUMAX<sup>3</sup> simulation ( $\theta, H$ )-mapping of Néel-type Skyrmions for sample D. Dotted lines indicate the  $\sim \pm 1/\cos(\theta)$  limits, and inset of (c) shows the deconvoluted two opposite-sign AHE loops. **(e, f)** Continuous hysteretic  $\theta$ -rotation Hall data for samples C,D.

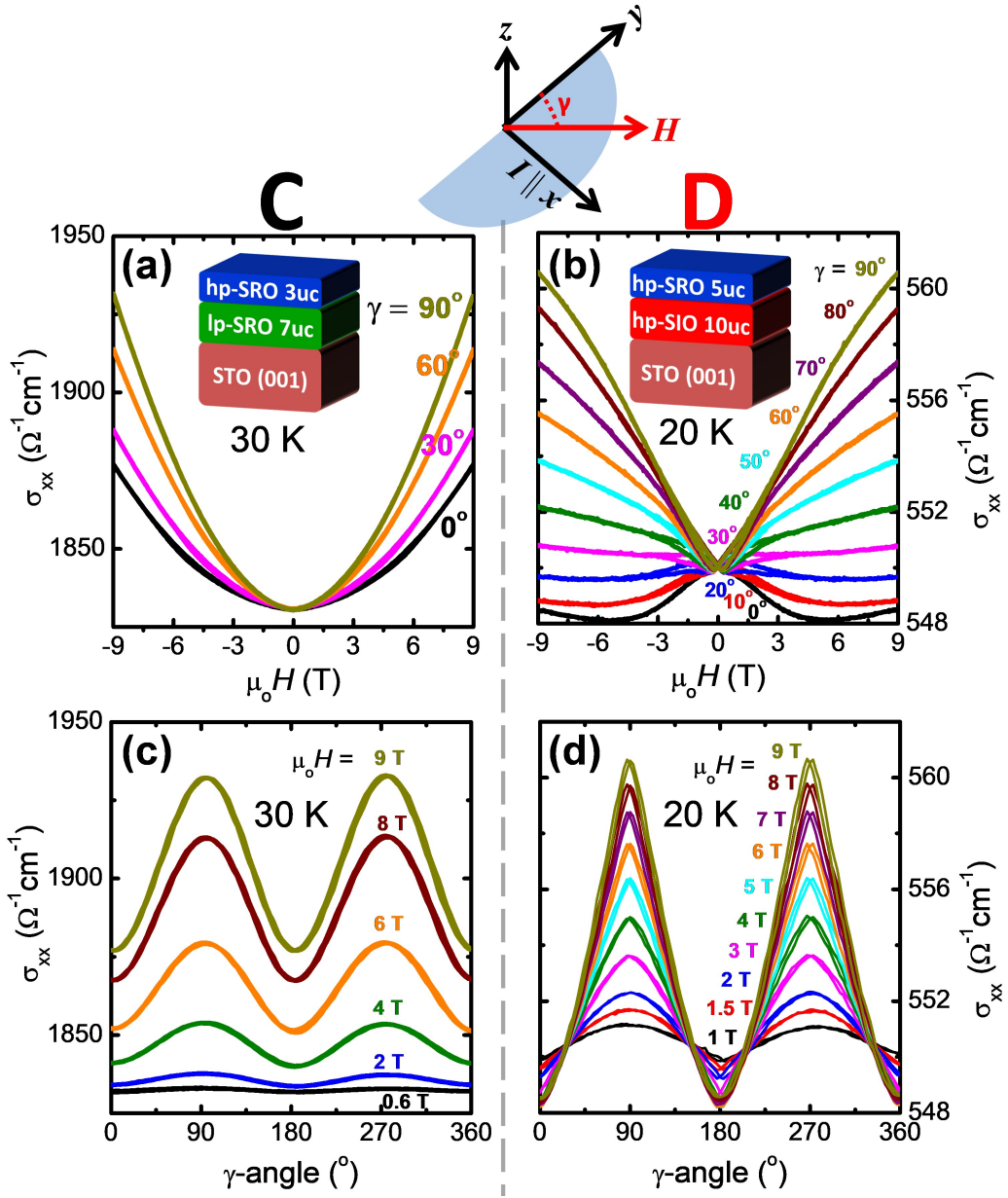


**Figure 3: Top panel:** Sketch of rotating-field linear conductivity measurement configuration  $\rho_{xx}(\gamma, H)$ . **(a, b)** Hysteretic magnetoconductivity data with varying  $\gamma$ -angle for samples C,D. **(c, d)** Continuous hysteretic  $\gamma$ -rotation magnetoconductivity data with varying fields for samples C,D.

## **Supplementary Information: Crossover from Karplus-Luttinger to Topological Hall**

### **Effects in SrRuO<sub>3</sub>-based heterostructures**

Hall-bars were defined by insulating amorphous AlN film with thickness ~250 nm on the STO(001) substrate with photolithography prior to crystalline film growths. All films have minimal surface roughness of ~rms. 0.15 nm without island growth (step-flow and layer-by-layer for SRO and SIO respectively), proving high quality interfaces.

In supplementary Fig. S1a, the half-integer XRD peaks of sample A to E are shown, with notations and HKL-indices following the Glazer's rules[1,2]. The substrate is STO(001) imposing an in-plane compressive strain to both SRO and SIO films, whose bulk materials belong to the *pbnm* space group with  $a^-a^-c^+$  – one in-phase rotation axis. In this class of materials, since the in-phase (+) oxygen octahedral rotation axis will shorten the B-O-B bond length, it is energetically favourable for the in-phase rotation axis to align with the equivalent in-plane compressive axes “*a*” or “*b*”[3]. Hence,  $a^-a^-c^+$  should not occur in our cases, while  $a^-b^+c^-$  and  $a^+b^-c^-$  may occur with equal probability[3-5]. This is consistent to the hp-SRO film showing peaks with equal magnitude at HKL=(0.5,0.5,1.5) and (1.5,0.5,1.5), proving the existence of strong  $a^-$ . The presence of a peak at (0.5,0,1.5) supports  $b^+$  and rules out  $b^-$ , hence  $c^-$  can be deduced from (0.5, 1.5,1.5), and forming  $a^-b^+c^-$ . We believe that the humps around (0.5,1.5,1) are measurement artifacts.

In sample B, most peaks are suppressed, consistent to tetragonal  $a^0a^0c^0$  of the lp-SRO phase which is also partially stabilized by oxygen vacancies[6]. Nevertheless, a sharp peak occurs at exactly (0.5,0.5,1.5), possibly due to defects. Similarly, all peaks are suppressed in sample C due to the dominant lp-SRO and small overall thickness. The tilt/rotation patterns and their gradual transformation in sample D are shown in Fig. S1b. After relaxing from suppression of tilt/rotation by the substrate, the  $a^+$  or  $b^+$  likely to form. Hence, the peak at (0,0.5,1.5) belongs

to the  $a^+$  of the bottom hp-SIO film. In fact, the hp-SIO film was deliberately designed to be thick enough for strain and tilt-suppression to relax. This way, the SIO film near the SRO/SIO interface can be assigned to  $a^+b^0c^0$ . Subsequently, the top SRO can be expected to have weak  $a^-b^+c^0$ , bearing much resemblance to the thick hp-SRO of sample A with  $a^-b^+c^-$ . However, if using the lp-SIO as the bottom buffer for the case of sample E, relaxation from suppression does not occur within the 10 uc thickness since oxygen vacancies tend stabilize tetragonal crystal structure. This results in total suppression of tilt/rotation including the top SRO, although a defect peak occurs again at (0.5,0.5,1.5). Comparing between the sample D and E from aspects of Hall Effects (main text Fig. 1d and Fig. S1c) and tilt/rotation details (Fig. S1a), we infer that the octahedral tilts and their abrupt change across the interface of sample D play a crucial role in producing the THE signal.

in Fig. S2a,b, the coercive fields ( $H_c$ ) of thick hp-SRO (Fig. S2a) and thick lp-SRO (Fig. S2b) measured from AHE, MR butterfly peaks and magnetometry are compared. The diverging  $H_c$  trends with  $\theta$  are fitted with  $\sim 1/\cos^\alpha(\theta)$  to get the exponents of  $\alpha=0.37$  and 0.62 respectively. In Fig. S2c, the Hall Effect with continuous magnetic field rotation in sample D were repeated in the xz-plane encompassing the current direction with rotation angle  $\beta$ , as well as varying temperatures, ie.:  $\rho_{xy}(\beta,H,T)$ . The fields were always swept from high field for ensuring saturation before reducing to the low field regime of the opposite direction to coincide with the the humps' peak-field ( $H_{peak}$ ), following the trend shown in main text Fig. 1d. The step functions occur in all curves at qualitatively the same  $\beta$ -positions as the  $\theta$ -positions reported in the main text Fig. 2f, suggesting the steps are universal with varying temperatures and independent of the current direction. In Fig. S2d,  $\rho_{xy}(\beta,H)$  was measured in sample E (absence of Hall-humps) by choosing varying low fields after sweep back from high saturation fields of the opposite directions, down to  $\pm 0.2$  T in the hysteresis regime, with

reference to Fig. S1c. No step function can be found in all curves, providing an evidence that the steps found in sample D can be pinpointed as a specific property of the THE humps.

In Fig. S3, the magnetometry data for sample C and D are shown, including the information of anisotropy with two field direction  $\mathbf{H}||\mathbf{c}$  (out-of-plane) and  $\mathbf{H}||\mathbf{a}$  (in-plane). Curie temperatures ( $T_C$ ) of  $\sim 125$  K and  $\sim 100$  K can be inferred from the moment versus temperature ( $M-T$ ) curves for C and D respectively (Fig. S3a,c). The field-cooling (FC)  $M-T$  curves of sample D extending to higher temperature cut-offs ( $\sim 150$  K) than the zero-field-cooled (ZFC)  $M-T$  curves are likely due to the proximity-induced magnetism and spin-liquid behaviour of SIO film. In Fig. S3b,d, the  $M-H$  hysteresis loops at the chosen temperature and the saturation magnetization  $M_{\text{sat}}$  with varying temperatures are shown. Information in Fig. S3 altogether are useful for extracting the micromagnetic simulation parameters for MUMAX<sup>3</sup> for sample D, using the following equations:

$$M_{\text{sat}} = 1.985 \times 10^5 \text{ A/m} \text{ (measured at 20 K)}$$

$$J_{\text{ex}} = \frac{3k_B T_C}{2j(j+1)} ; A_{\text{ex}} = J_{\text{ex}}/a = 2.628 \times 10^{-12} \text{ J/m}$$

$$l_{\text{ex}} = \sqrt{\frac{2A_{\text{ex}}}{\mu_0 M_{\text{sat}}^2}} = 10.3 \text{ nm}$$

$$K_u = \int_0^{H_{\text{sat}}} (M_{H||c} - M_{H||a}) \cdot dH = 2.481 \times 10^4 \text{ J/m}^3$$

where  $J_{\text{ex}}$ ,  $A_{\text{ex}}$ ,  $l_{\text{ex}}$  and  $K_u$  are the exchange constant, exchange stiffness, exchange length, and uniaxial magnetic anisotropy respectively.  $j=1$  is the total angular momentum quantum number since 4d<sup>4</sup> electronic configuration is arguably lying between the weak SOC (l-s coupling) and strong SOC (j-j coupling) regimes, with  $S=1$ ,  $L=1$ , and  $\mathbf{J}=\mathbf{L}+\mathbf{S}=1$  because the two vectors are neither parallel nor antiparallel. “a” is the pseudocubic lattice parameter 3.94 Å. Justifiably, we use a cell size of 4 nm  $< l_{\text{ex}}$ , with 256x256 meshes in the xy-plane but 1-

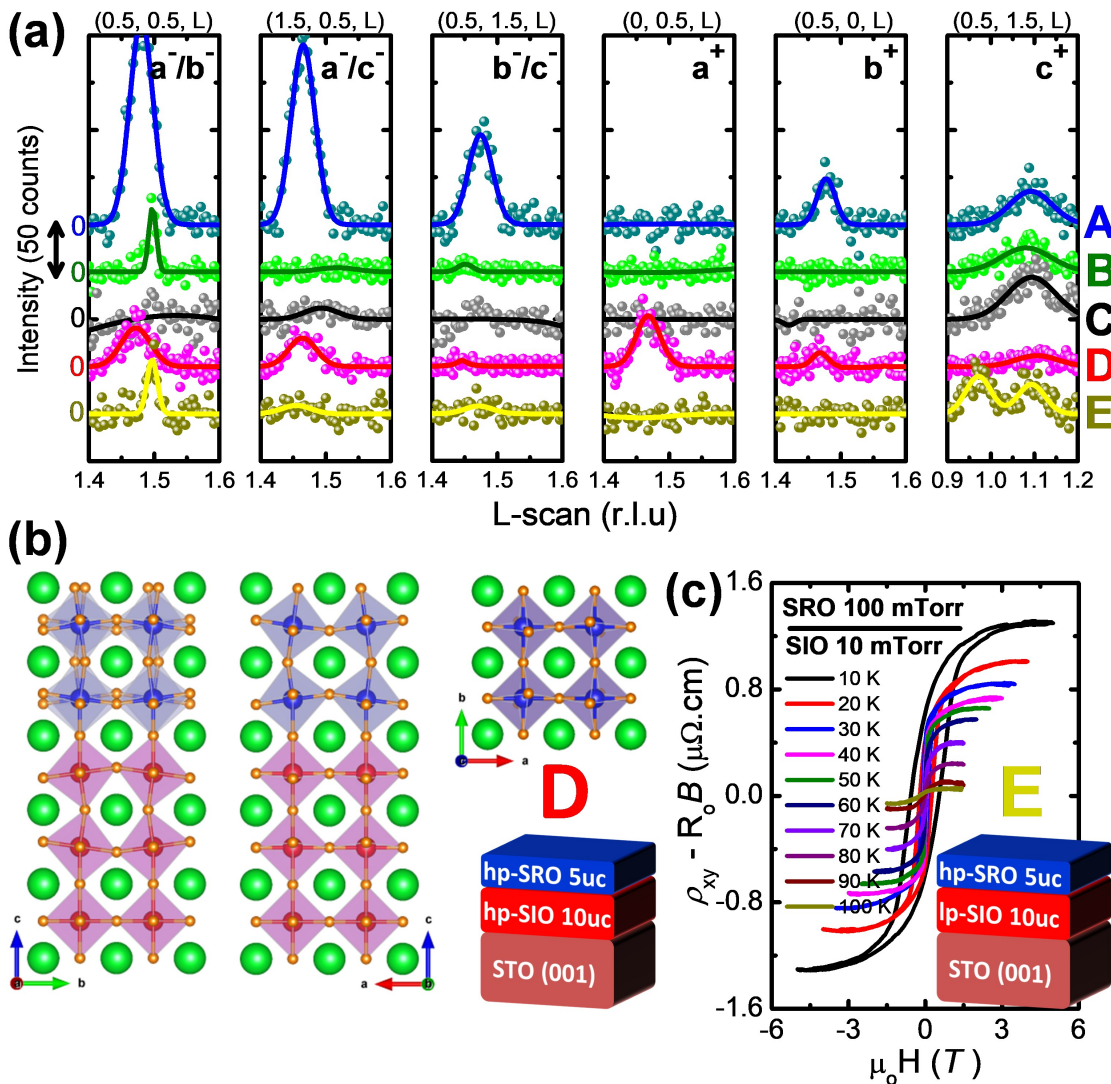
cell in the z-direction thickness. The Gilbert damping constant,  $\alpha_G$  is reasonably set to 0.7 following a past publication[7] about ferromagnetic resonance of SRO. The DMI  $D_{\text{ind}} = 1.85 \times 10^{-3}$  J/m<sup>2</sup> induced at the SRO/SIO interface was optimized (as a free parameter) to match the  $\mu_0 H_{\text{peak}} = 1$  T in Hall effect of sample D at 20 K. While the backward/forward field sweep simulations are always initialized with  $m=\text{Uniform}(0,0,\pm 1)$  to retain the history of magnetization saturation. Each simulation was terminated after reaching a criterion of max-torque  $< 5 \times 10^{-3}$ . We notice that  $K_u = 1.08 \times 10^5$  J/m<sup>3</sup> of sample C is far larger than that of sample D, which offers another clue that it is unlikely to stabilize magnetic Skyrmions.

Fig. S4 shows the MUMAX<sup>3</sup> simulation results for *TCD* varying with sweeping field at  $\theta=0$  (Fig. S4a), as well as the snapshots of real-space moment alignment at particular  $(\theta,H)$  parameters within the mapping of main text Fig. 2e (Fig. S4b). Along the middle column where  $\theta$  is increased at the field with the maximum *TCD*, the Néel-type Skyrmions are progressively converted back into stripes[8,9], but they are oriented more uniformly along a particular in-plane (y-) direction, unlike the stripes in the snapshots at  $H=0$ . This agrees with the argument about “triple-*q* distorted by in-plane field” highlighted in the main text.

## References:

- [1] Glazer, AcCrB **28**, 3384 (1972).
- [2] Glazer, AcCrA **31**, 756 (1975).
- [3] van Thiel *et al.*, ACS Materials Letters **2**, 389 (2020).
- [4] Nie *et al.*, Phys. Rev. Lett. **114**, 016401 (2015).
- [5] Schütz *et al.*, Phys. Rev. Lett. **119**, 256404 (2017).
- [6] Lu *et al.*, Phys. Rev. B **88**, 214115 (2013).
- [7] Langner *et al.*, Phys. Rev. Lett. **102**, 177601 (2009).
- [8] Leonov *et al.*, Phys. Rev. B **96**, 214413 (2017).
- [9] Wan *et al.*, Phys. Rev. B **99**, 180406 (2019).

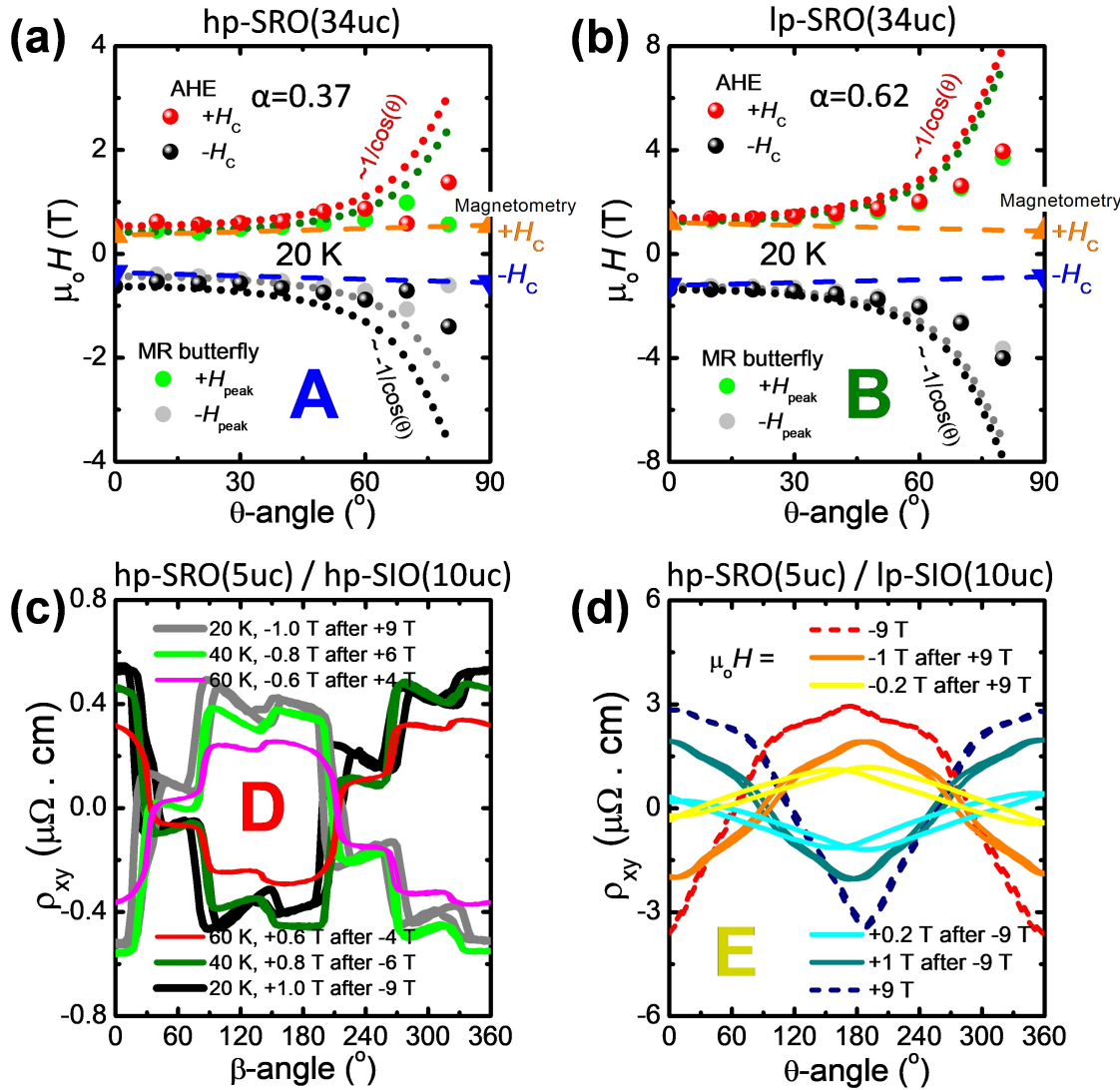
**Supplementary Figures:**



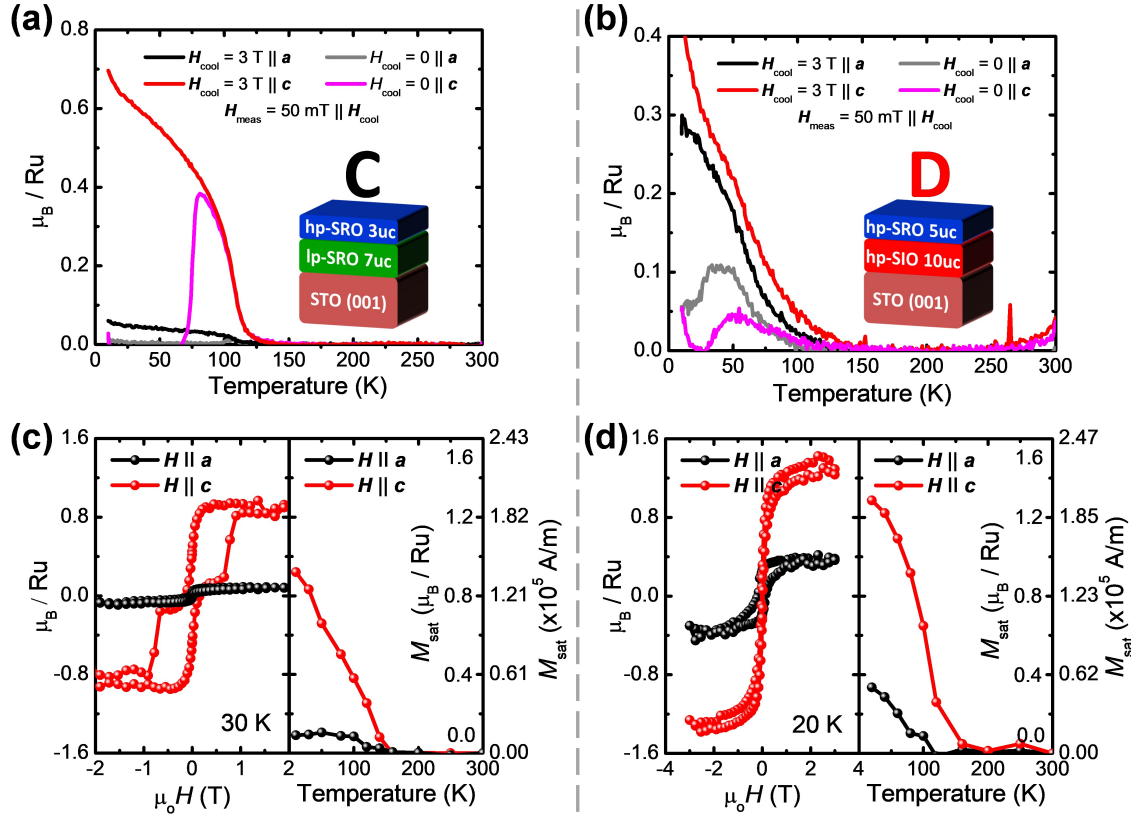
**Supplementary Figure S1: (a)** Half-integer X-ray Bragg diffraction data for sample A to E.

**(b)** Illustrations of octahedral tilts and rotation of sample D generated by Vesta, as viewed from the  $a$ ,  $b$  and  $c$  directions. Red, blue, green and orange spheres represent  $\text{Ir}^{4+}$ ,  $\text{Ru}^{4+}$ ,  $\text{Sr}^{2+}$  and  $\text{O}^{2-}$  ions respectively, while the oxygen octahedral cages are shaded as guide-to-the-eyes.

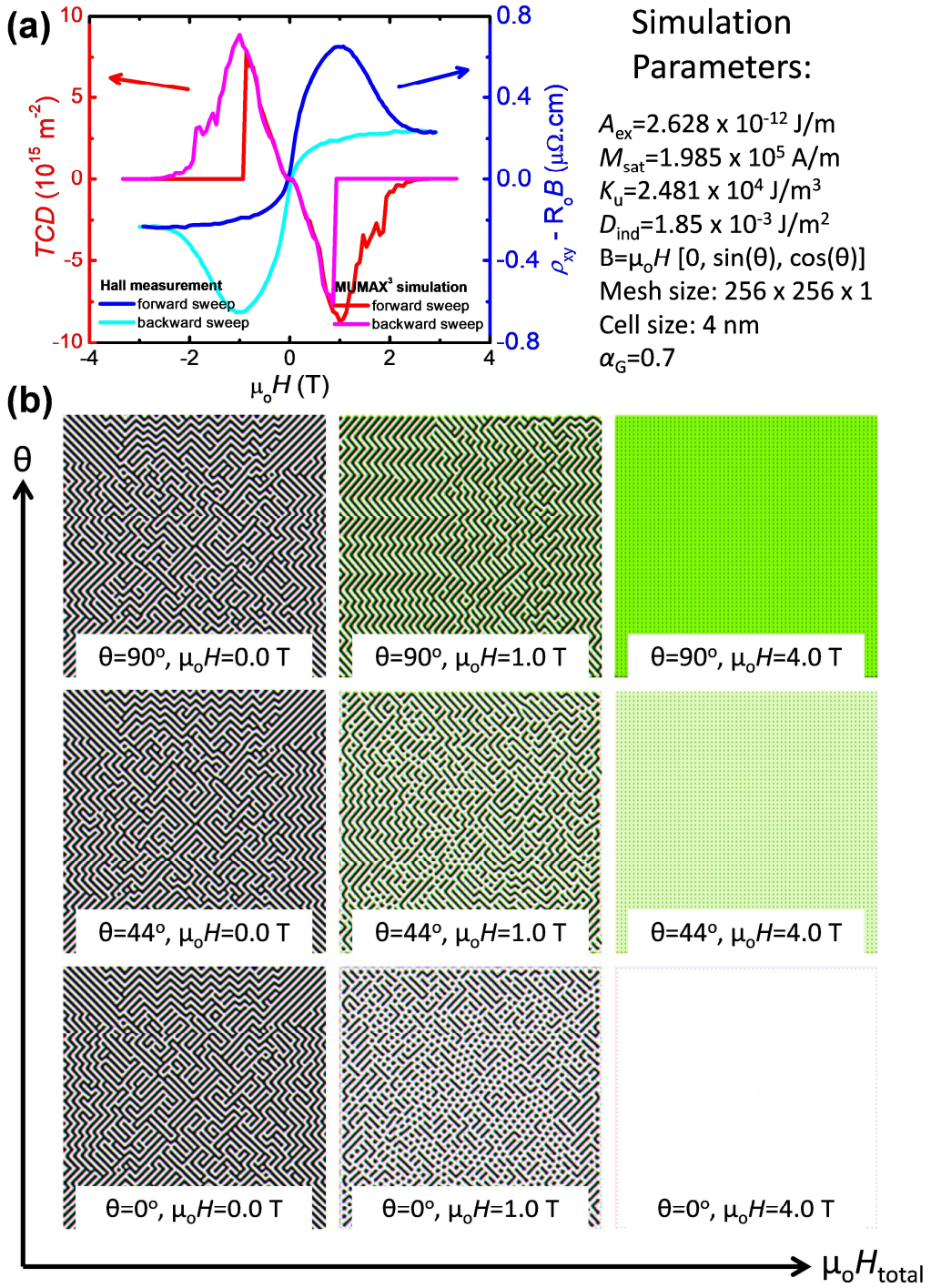
**(c)** Hall Effect data of sample E with varying temperatures.



**Supplementary Figure S2:** Analyses of  $H_c$  varying with  $\theta$  for **(a)** sample A and **(b)** sample B respectively. The  $H_{\text{peak}}$  under “MR butterfly” is just equivalent to  $H_c$  and does not refer to the  $H_{\text{peak}}$  of Hall Effect in sample C and D. **(c)**  $\rho_{xy}(\beta, H)$  data of sample D at low-fields after opposite-field saturation and at varying temperatures, with definition of  $\beta=0^{\circ}$  at  $\mathbf{H}||z$  and  $\beta=90^{\circ}$  at  $\mathbf{H}||x$  parallel to the current direction. **(d)**  $\rho_{xy}(\theta, H)$  data of sample E with varying low fields after saturation. Dashed curves indicate measurements at saturation fields.



**Supplementary Figure S3:**  $M-T$  curves of **(a)** sample C and **(b)** sample D respectively. The  $M-H$  loops (left panels) and  $M_{\text{sat}}$  extracted from  $M-H$  loops with varying temperatures (right panels) are shown in **(c)** for sample C and **(d)** for sample D respectively.



**Supplementary Figure S4:** (a) MUMAX3 simulation results for TCD versus sweeping magnetic field at  $\theta=0$  (red and pink curves), overlapped onto the Hall data (blue and cyan) for comparison. (b) Snapshots at selected  $(\theta, H)$  values in the main text Fig. 2e mapping. All simulations follow the same parameters as given at the right panel of (a).